Advanced Powder Technology 33 (2022) 103581

Contents lists available at ScienceDirect

Advanced Powder Technology

journal homepage: www.elsevier.com/locate/apt

Synthesis of macroporous three-way catalysts via template-assisted spray process for enhancing mass transfer in gas adsorption

Phong Hoai Le [a], Yasuhiko Kitamoto [a], Kiet Le Anh Cao [a], Tomoyuki Hirano [a], Eishi Tanabe [b], Takashi Ogi [a,*]

[a] Chemical Engineering Program, Department of Advanced Science and Engineering, Graduate School of Advanced Science and Engineering, Hiroshima University, 1-4-1 Kagamiyama, Higashi-Hiroshima City, Hiroshima 739-8527, Japan
[b] Western Region Industrial Research Center, Hiroshima Prefectural Technology Research Institute, 3-13-26 Kagamiyama, Higashi-Hiroshima City, Hiroshima 739-0046, Japan

ARTICLE INFO

Article history:
Received 15 February 2022
Received in revised form 6 April 2022
Accepted 14 April 2022

Keywords:
Nanostructured particles
Three-way catalysts particles
Template-assisted aerosol process
CO_2 adsorption rate
Mass transfer coefficient

ABSTRACT

Catalyst particles with macroporous structures have been attracting much attention because of their high molecular diffusions and catalytic activities. In this study, macroporous-structured three-way catalyst (TWC) particles were synthesized via a template-assisted spray process followed by an additional heating process. Several process parameters, i.e., carrier-gas type, template size, and reaction temperature, were investigated to enable preparation of macroporous particles with controllable porous structures and interconnected pore networks. The mass transfer coefficients of the obtained macroporous TWC particles were assessed using the Linear Driving Force approximation to understand the effects of the macroporous structure on the mass transfer improvement. The results showed that the introduction of macropores into TWC particles enhances the mass transfer coefficient.

1. Introduction

A heterogeneous catalyst is one kind of catalysts, where its phase differs from those of reactants and products [1]. Heterogeneous catalysts have a wide range of applications because this phase difference enables easy removal and recovery of the catalyst from the mixtures after reactions [2–4]. However, the activation of a heterogeneous catalytic process requires a large amount of energy [5]. It is therefore essential to boost the catalytic activity to minimize energy consumption and the environmental impact. Many previous studies have shown that the introduction of porous structures improves the catalytic performance [6–8]. Porous structures are getting a lot of attraction from scientists because of their ability to interact with the reactants, adsorbents, ions, and atoms on their surfaces and interiors. The pore classifications are identified according to their size: the pores with size below 2 nm are called micropores, those in size range of 2–50 nm are denoted as mesopores, and those above 50 nm are macropores [9].

Macroporous structures are highly attractive in many applications, e.g., photocatalytic, electrocatalytic, adsorption, and energy storage applications, because of their high mass transfer efficiencies [10–12]. In terms of photocatalytic applications, Iskandar et al. and Arutanti et al. produced the macroporous structures that improve the photocatalytic performances of TiO_2 and WO_3/Pt catalysts [13–15]. The organic compound photodegradation activities under visible light of the prepared macroporous catalysts showed five to ten times higher than those of dense and nanostructured catalysts. Regarding electrocatalytic applications, Balgis et al. used an aerosol method to synthesize the macroporous carbon-supported Pt particles with enhanced electrocatalytic activities [16–18]. These results indicated that the macroporous structures can allow high Pt loading and improve the electrocatalytic performance as a result of their greater active surface area and mass transfer promotion. In terms of adsorption, Rahmatika et al. prepared the macroporous particles by aerosol spray method for protein adsorption [19–21]. These macroporous particles exhibited excellent protein adsorption capacities and gave rapid adsorption rates because the macroporous structure promoted the protein transportation. Furthermore, Zheng et al. prepared three types of porous catalysts, namely mesoporous, micro-mesoporous, and micro-meso-macroporous structures, for electrochemical performances [22]. The results demonstrated that lithium-storage performances were enhanced by the introduction of macroporous structures. These improvements in material performances arise from the mass transfer enhancement by the macroporous structures, where reactants or adsorbates are quickly transported from the outer surface into the inner pores of the structures [23]. The attractive advantages of the macroporous structures suggest that

* Corresponding author.
E-mail address: ogit@hiroshima-u.ac.jp (T. Ogi).

https://doi.org/10.1016/j.apt.2022.103581

the concept "introduction of macroporous structure" would be able to utilize in other functional powder materials.

Three-way catalyst (TWC) is a crucial and efficient material, which is utilized in vehicle's aftertreatment systems to reduce hydrocarbon, CO, and NO_x emissions into the environment [24–26]. These three primary exhaust components can be simultaneously converted to CO_2, H_2O, and N_2 by the catalysis of platinum group metals (PGM) in TWC [27]. The PGM components are anchored to the strong stabilizers, i.e., Al_2O_3 and $Ce_xZr_{1-x}O_2$, because of their excellent thermal stabilities and oxygen storage capacities [28,29]. Until now, the TWC materials have been adequate for achieving removal of harmful gases to meet current emission regulations. However, governments across the world continue to issue new regulations with lower emission limits to minimize the adverse impacts on human health and the environment of air pollution caused by exhaust emissions [30]. Therefore, finding an efficient utilization of TWC to improve its catalytic performance is still a challenge, and macroporous-structured TWC is expected to achieve this goal.

Based on the above background, this study focused on the preparation of the macroporous TWC particles. Macroporous TWC particles were synthesized via a template-assisted spray approach [31,32] with subsequent additional heating process, and the assistance of a poly(methyl methacrylate) (PMMA) as a template. As preliminary experiment, this paper focused on investigating the effects of important experimental parameters, i.e., carrier-gas type, reaction temperature, and template size on the preparation of macroporous TWC particles. In addition, the effectiveness of the macroporous structure of the TWC particles was investigated by using the Linear Driving Force (LDF) approximation to assess their mass transfer coefficients. To the best of our knowledge, this is the firstly reported study focused on synthesizing macroporous TWC particles to improve their mass transport efficiency.

2. Materials and methods

2.1. Materials

Macroporous TWC particles were prepared from precursor solutions containing TWC nanoparticles and commercial PMMA particles in deionized water. The raw TWC sample with particle size of 8 ± 3 nm, which was counted approximately 150 particles from transmission electron microscopy (TEM) images, is shown in Figure S1(a) (Supplementary material). Figure S1(b) and (c) (Supplementary material) show the morphologies of two kinds of PMMA (i.e., 67 ± 8 and 242 ± 14 nm, respectively) and their particle size distributions, which were obtained by counting approximately 300 particles from scanning electron microscopy (SEM) images. A slurry containing 20 wt% of TWC nanoparticles was obtained from the Mitsui Mining & Smelting Co., ltd., Tokyo, Japan. Commercial PMMA particles were obtained as powders from the Sekisui Plastics Co., ltd., Tokyo, Japan. Deionized water was used as the solvent in all experiments.

2.2. Preparation of macroporous TWC particles

Prior to the experiments, the precursor solutions were ultrasonicated for several minutes at room temperature to ensure homogeneous dispersion of the TWC and PMMA particles. The TWC concentration was set at 1.0 wt% under all conditions, and two types of PMMA (i.e., 67 and 242 nm) were used at a PMMA/TWC mass ratio of 1.0. A control sample without PMMA (denoted by **P0-TWC**) was prepared under the same conditions for comparison with the macroporous TWC particles.

The precursor solutions were then introduced into the spray apparatus; a schematic diagram of the set-up is shown in Fig. 1 **(a)**. A more detailed description of the components and mechanism of the spray method are available in a previous publication [33]. Briefly, the precursor solutions were pumped into an ultrasonic nebulizer (NE-U17, Omron Healthcare Co., ltd., Kyoto, Japan, operated at 1.7 MHz), in which droplets were generated. The droplets were then transported by the carrier gas through a ceramic furnace (diameter 12 mm, length 1500 mm) with four temperature zones set at 250, 350, 500, and 500 °C, respectively. Nitrogen (N_2) or air was used as carrier gas at a flow rate of 2 L min^{-1}. The final products were then obtained from a glass fiber filter, which was heated at 150 °C to prevent water condensation. All samples were denoted by ***A*-TWC-*B***, where ***A*** represents the PMMA types (***A* = P1** and **P2** for samples prepared from PMMA 67 and 242 nm, respectively) and ***B*** indicates the carrier-gas type (***B* = A** for air and **blank** for N_2). The effects of the carrier-gas type on the particle morphology were investigated by preparing a TWC/PMMA composite under the following conditions: PMMA 242 nm were used at a PMMA/TWC mass ratio of 1.0; the four temperature zones were set at 150, 300, 300, and 300 °C, respectively; and N_2 at a flow rate of 1 L min^{-1} was used as the carrier gas. Another macroporous sample was prepared from a PGM-free TWC and PMMA 242 nm in an air flow as the carrier gas (denoted by **P2-WP-A**) to investigate the effects of the PGM on the PMMA decomposition rate in air. After preparation of the macroporous TWC particles by the spray method, an additional heating process was required to completely remove the remaining PMMA from the products. The heating process was performed in a horizontal furnace (Fig. 1**(b)**), and the temperature was increased to 500 °C with the increasing step of 5 °C min^{-1} and kept for 1 h. Air was introduced 30 min prior to the heating process at a flow rate of 3 L min^{-1} to remove the other gases inside the furnace, and the gas flow rate was then set at 1 L min^{-1} during the heating process. All samples that had been subjected to the additional heating step are denoted by ***A*-TWC-*B*-*H***. Details of the precursor contents and spray conditions are given in Table 1.

2.3. Characterization of porous TWC particles

The morphologies of the as-prepared samples were examined by a field-emission SEM (FE-SEM; S-5200, 3–5 kV, Hitachi Corp., ltd., Tokyo, Japan) and a TEM (JEM-2010, 200 kV, JEOL Corp., ltd., Tokyo, Japan). TEM Tomography and energy dispersive X-ray spectroscopy (EDS) element mapping of the prepared samples were performed at an accelerating voltage 297 kV (JEM-3000F, JEOL Corp., ltd., Tokyo, Japan). Three-dimensional (3D) reconstruction and visualization were performed with TEMography software (SYSTEM IN FRONTIER Inc.). The crystal structures of the prepared particles were determined by X-ray diffraction (XRD; D2 PHASER, Bruker Corp., Billerica, MA, USA). The decomposition and remaining amounts of PMMA in the different types of carrier gas were analyzed by thermogravimetric analysis (TGA; TGA-50/51, Shimadzu Corp., Kyoto, Japan). The TGA was performed with N_2 or air at a gas flow rate of 50 mL min^{-1}, and the temperature was increased at a rate of 10 °C min^{-1}. The N_2 adsorption–desorption isotherms were conducted at 77 K using a BELSORP-max (MicrotracBEL Japan, Osaka, Japan); the specific surface area (SSA) and pore characteristics were determined by using Brunauer-Emmett-Teller, Barrett-Joyner-Halenda (BJH), and Horvath–Kawazoe methods. The CO_2 adsorption capacities and CO_2 adsorption rates were also performed at 298.15 K by using the BELSORP-max instrument. Mass transfer coefficients were determined from the CO_2 adsorption rate and by using the LDF approximation; details are available in a previous publication [34]. Briefly, the change in the adsorbed amount with time is written as.

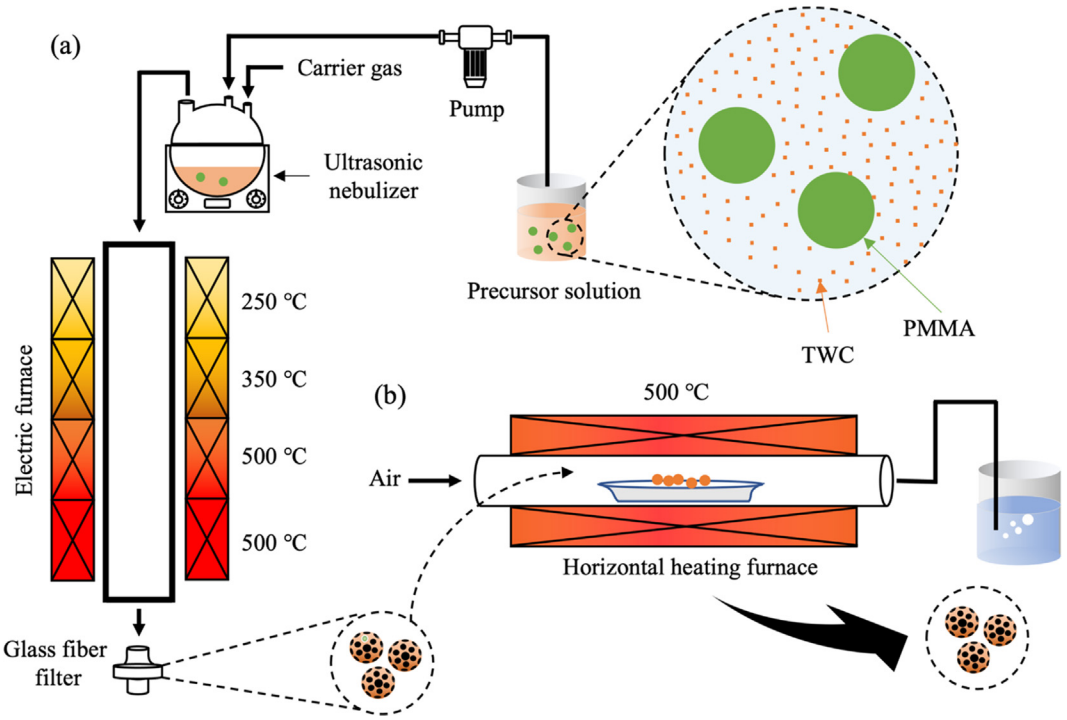

Fig. 1. Experimental set-up for spray method (a) and additional heating process (b).

Table 1
Conditions for synthesis of porous TWC particles.

Sample	TWC type	PMMA size [nm]	PMMA concentration [wt%]	Carrier gas
P0-TWC	With PGM	–	–	N_2
P1-TWC	With PGM	67	1.0	N_2
P2-TWC-A	With PGM	242	1.0	Air
P2-WP-A	Without PGM	242	1.0	Air
P2-TWC	With PGM	242	1.0	N_2

$$\frac{dC}{dt} = k_{LDF}(C_e - C)$$

where k_{LDF} is the particle mass transfer coefficient [s^{-1}], C_e is the adsorbed amount at equilibrium, and C is adsorbed amount at time t [s]. Integration of this equation with the boundary conditions, $t = 0$ and $C = C_0$ gives.

$$\ln\left(\frac{C - C_e}{C_0 - C_e}\right) = -k_{LDF} \times t$$

The particle mass transfer coefficient can be obtained from above equation. All samples were pretreated for 6 h at 110 °C under vacuum conditions to eliminate water.

3. Results and discussion

3.1. Morphology of porous TWC particles

The effects of the carrier-gas type on macroporous TWC particle formation are shown in Fig. 2. The SEM image in Fig. 2**(a)** demonstrates that the spherical and macroporous TWC particles were formed when the carrier gas was N_2. The macroporous particles formation using template in our study is consistent with previously reported results [18,32,33]. Fig. 2**(b)** shows that broken porous TWC particles were obtained when air was used as the carrier gas instead of N_2. For better understanding this phenomenon, the TWC/PMMA composite particles were prepared by a spray method at a low temperature. The SEM images of the TWC/PMMA composite (Fig. 2**(c)**) shows the spherical particles with some surface pores, which arise from partial decomposition of PMMA. The TWC/PMMA composite was then analyzed by TGA with different gases, as shown in Fig. 2**(d)**. The TGA curves show rapid decomposition of PMMA at 320 °C in air, but slow decomposition in N_2. These results show that the air atmosphere promoted decomposition of PMMA in the TWC/PMMA composite, and this resulted in particle breakage. The reason for promotion of PMMA decomposition might come from the catalysis of active components in TWC. A TWC material usually contains PGM components for the catalytic conversion and $Ce_xZr_{1-x}O_2$ as an oxygen storage material, which can adsorb and release oxygen for the reactions in the TWC system [28]. The PGM or $Ce_xZr_{1-x}O_2$ components in the TWC material could therefore promote the PMMA decomposition in air, with formation of broken TWC particles.

To identify which components in TWC promoted the PMMA decomposition in air, the same procedure was used to produce macroporous TWC particles (**P2-WP-A**) from a TWC material that did not contain PGM components. The SEM image of this sample (Fig. 3**(a)**) shows that spherical macroporous TWC particles were obtained in the absence of PGM components. The TGA curves in Fig. 3**(b)** show fast decomposition of PMMA in an air atmosphere

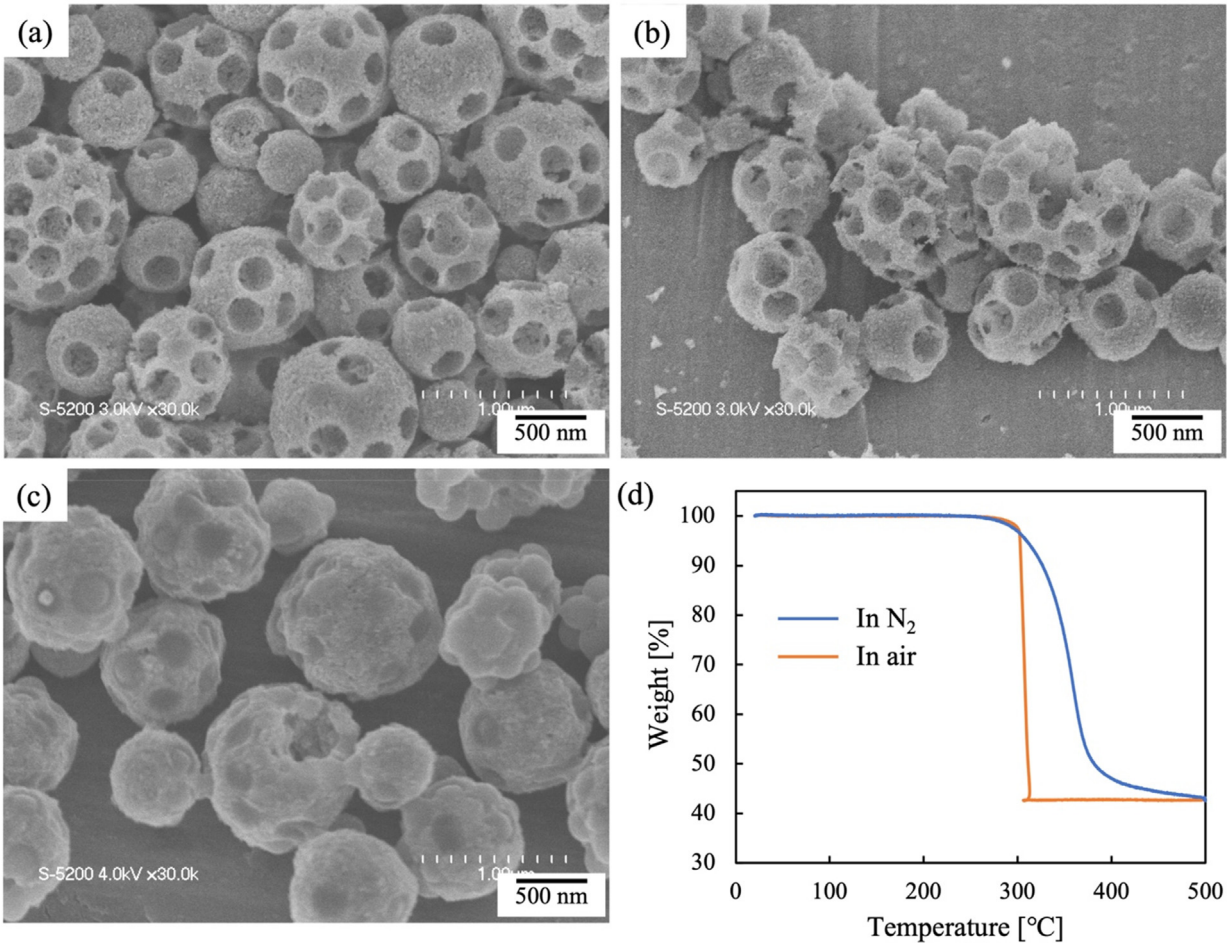

Fig. 2. SEM images of **P2-TWC** (a), **P2-TWC-A** (b), and prepared TWC/PMMA composite (c) and its TGA curves in N_2 and air atmospheres (d).

in the presence of PGM, but slow decomposition of PMMA for PGM-free TWC. The PGM components are therefore mainly responsible for fast decomposition of PMMA in air. Generally, Palladium (Pd) in PGM is used to promote the oxidation of the organic compounds in the exhaust emissions with the cooperation of oxygen in the air [35]. The presence of Pd component in the macroporous TWC particles was confirmed, as shown in **Figure S2** (Supplementary material). The oxidation of PMMA was therefore accelerated by the catalysis of Pd during template decomposition at high temperatures. Rapid decomposition of the template could lead to a massive gas release in a short time from the inside of the particle. This gas release could destroy the wall formed by TWC nanoparticle aggregations, which would result in the broken particles. Based on above results, Fig. 3**(c)** proposes the formation mechanisms of macroporous TWC particles derived from TWC materials with and without PGM in air as carrier gas. Briefly, after the water has evaporated from the droplets, spherical TWC/PMMA composite particles are obtained. For TWC that contains PGM, the PGM component catalyzes PMMA decomposition in air, and then large quantities of gas from the PMMA decomposition process are released in a short time. The large amount of gas destroys the TWC wall, which results in particles breakage. Meanwhile, in case of TWC without PGM, the PMMA decomposition rate is low, and the gas is slowly released from the TWC particles. Spherical TWC particles are obtained from the PGM-free TWC even though the presence of oxygen in process. In conclusion, spherical macroporous TWC particles were successfully prepared by using N_2 as the carrier gas in the case of PGM-containing TWC materials.

The TGA curve of TWC/PMMA composite in a N_2 atmosphere shows the continuous reduction up to 500 °C, indicating the spray temperature was insufficient for the complete PMMA decomposition. The TGA results in Fig. 2**(d)** also show that PMMA was completely decomposed before 500 °C in air. Therefore, an additional heating step in air was required to completely remove the PMMA from the prepared macroporous TWC particles after the spray process. However, prolonged heating at a high temperature decreases the TWC surface area and activity because of migration and incorporation of the PGM components in the TWC materials [36,37]. The temperature for the additional heating step was therefore set at 500 °C in an air atmosphere. Fig. 4 shows the morphologies of the TWC particles prepared with and without a template as well as before and after the additional heating process. Fig. 4**(a)** shows SEM and TEM images of the spherical and aggregate TWC particles that were obtained in the absence of PMMA. Spherical and macroporous particles were formed in the presence of PMMA, as shown in Fig. 4**(b)** and **(c)**. These results demonstrate that the spherical morphology was retained during the change from an aggregate structure to a macroporous structure by addition of PMMA as a template. Furthermore, the morphologies of the prepared TWC particles were retained during the additional heating process both without (Fig. 4**(a-1)** and **(a-2)**) and with (Fig. 4**(b-1)**, **(b-2)** and **(c-1)**, **(c-2)**) template. Because most of the PMMA had decomposed during the spray process, not much gas was released during the additional heating process, therefore no broken particles were obtained. However, the particle sizes of all the samples decreased during the additional heating process because of particle shrinkage

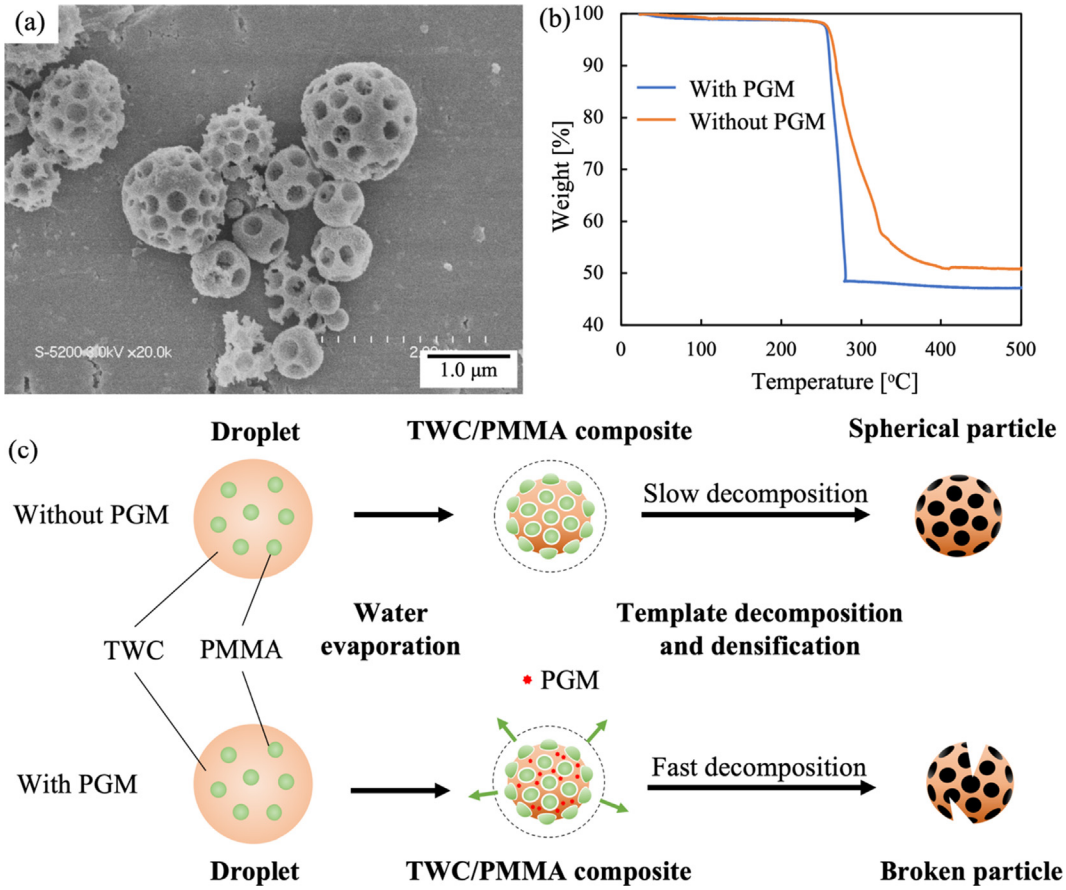

Fig. 3. SEM images of **P2-WP-A** (a), TGA curves of mixtures of TWC with and without PGM, and PMMA 242 nm in air (b), and proposed mechanisms of macroporous TWC particle formation from TWC materials with and without PGM using air as carrier gas (c).

at high temperatures [38]. Specifically, additional heating caused a decrease in the particle size of the aggregate TWC particle (**P0-TWC**) from 629 to 590 nm. Similar reductions in the particle sizes also occurred for the **P1-TWC** and **P2-TWC** samples, from 778 to 733 nm and from 859 to 805 nm, respectively. Because of the presence of the macropores, the macroporous TWC particles were larger than the aggregate particles. In a comparison of the results achieved with two different template sizes, i.e., 67 and 242 nm, the larger template provided the larger particle diameter. The TEM images in Fig. 4**(a-3)**-**(c-3)** show the internal structures of the porous TWC particles. In the absence of a template, the spherical aggregate TWC particles were obtained by aggregations of TWC nanoparticles (Fig. 4**(a-3)**), whereas use of PMMA as a template gave spherical TWC particles with homogeneously distributed macropores (Fig. 4**(b-3)** and **(c-3)**).

An interconnected pore structure increases the mass transfer efficiency [12,39]. Molecules easily penetrate from the outer surface to the interior structure through the interconnected pore network. The internal structure of the macroporous TWC particles was clarified by using TEM Tomography analysis to measure the interior structure and construct a 3D structural representation. TEM Tomography volume rendering videos of two samples derived from PMMA of different sizes, i.e., 67 nm (**P1-TWC-H**) and 242 nm (**P2-TWC-H**), are shown in **Videos S1** and **S2** (Supplementary videos), respectively. Images of the 3D structures of **P1-TWC-H** and **P2-TWC-H** are shown in Fig. 5. The images of the 3D structure of the macroporous TWC sample derived from PMMA 67 nm (Fig. 5**(a-1)**) shows an association of macropores and an interconnected pore structure. The slice image of this sample in Fig. 5**(a-2)** shows the macropore distributions inside the structure; these macropores are connected to form an interconnected pore network inside the particle. Fig. 5**(b-1)** shows the 3D structural images of the macroporous TWC sample derived from PMMA 242 nm; the interconnected pore structure is more straightforward to be observed. The slice image of this sample (Fig. 5**(b-2)**) shows the distributions of the macropores inside the particles and the presence of some voids between them. These voids are formed via the connections between two adjacent macropores. Molecules can easily penetrate deeper into the inner structure of the particle through these voids. These results show that the macroporous TWC particles derived from PMMA 242 nm possess an interconnected pore network. In conclusion, use of PMMA 67 and 242 nm with PMMA/TWC at a mass ratio of 1.0 can generate macroporous particles with interconnected pore structures.

The effectiveness of the additional heating process was confirmed by using TGA to determine the amounts of PMMA remaining in the samples before and after additional heating. After the additional heating process, PMMA had been completely eliminated from the macroporous TWC particles (**Figure S3(a)**, Supplementary material). XRD measurements were also performed to determine the TWC crystal structures after the spray and additional heating processes. The results (**Figure S3(b)**, Supplementary material) show that the crystal structures were retained after the preparation, which indicates that the porous TWC particles possess similar catalytic performances. Full details of the TGA and XRD results are given in Supplementary material.

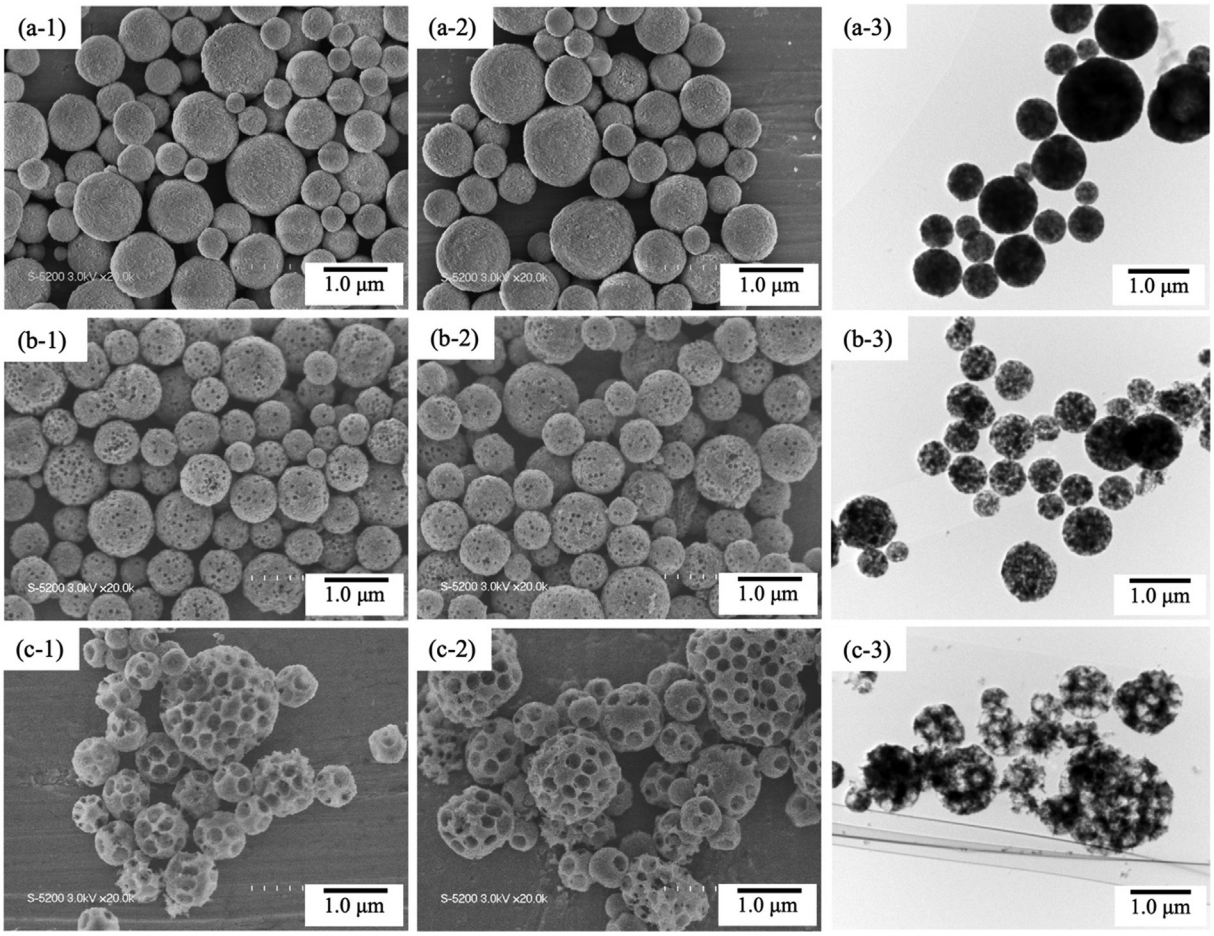

Fig. 4. SEM images (left) of **P0-TWC** (a-1), **P1-TWC** (b-1), and **P2-TWC** (c-1) samples before heating process, SEM (middle) and TEM (right) images of **P0-TWC-H** (a-2, a-3), **P1-TWC-H** (b-2, b-3), and **P2-TWC-H** (c-2, c-3) samples after heating process.

3.2. Gas adsorptions of porous TWC particles

N_2 adsorption–desorption isotherms were measured and used to evaluate the physical properties of the porous TWC samples (Fig. 6**(a)**). The sample prepared in the absence of PMMA (**P0-TWC-H**) exhibits a type IV isotherm with a hysteresis loop at high relative pressures (P/P_0 > 0.7); this is characteristic of a mesoporous structure [40]. The N_2 adsorption–desorption isotherms of the samples prepared with PMMA (**P1-TWC-H** and **P2-TWC-H**) possess type II isotherms with hysteresis loops at high relative pressures; these indicate the characteristic of a macroporous structures [41]. The significant increases of N_2 adsorption capacities at the low relative pressures (P/P_0 < 0.01) as well as the slow increases at medium relative pressures demonstrate the presence of microporous structures in these TWC particles [42,43]. More details of the pore size distributions of **P0-TWC-H**, **P1-TWC-H**, and **P2-TWC-H** are shown in Fig. 6**(b)**. The **P0-TWC-H** sample possesses mesopores, which are constructed by aggregation of TWC nanoparticles. The macroporous TWC particles derived from PMMA 67 nm possess a macropore peak at 124 nm, and the obtained macropore size is larger than the template size because of the connections between macropores in the particles. A macropore peak is not observed in the **P2-TWC-H** pore size distribution (Fig. 6**(b)**) because the obtained macropores are larger than 200 nm, and their sizes cannot be determined by the BJH method.

The data presented in Table 2 show that the samples prepared without a template possesses a SSA of 100 $m^2\ g^{-1}$, and its mesopore volume (0.259 $cm^3\ g^{-1}$) was abundant compared with micropore volume (0.037 $cm^3\ g^{-1}$), and macropore volume (0.025 $cm^3\ g^{-1}$). When PMMA 67 nm was used as a template, macropores were formed and the macropore volume increased (0.136 $cm^3\ g^{-1}$); the mesopore volume was maintained at 0.271 $cm^3\ g^{-1}$. The mesopore volume of macroporous TWC particles derived from PMMA 242 nm was similar to that of the sample prepared without a template. This indicates that the macropores did not occupy mesopores in the structure. The mesopore volumes of the macroporous samples (**P1-TWC-H** and **P2-TWC-H**) were therefore similar to that of the aggregate sample (**P0-TWC-H**). The micropore volumes of all the samples prepared with and without PMMA remained at approximately 0.037–0.041 $cm^3\ g^{-1}$. Because the micropore and mesopore volumes were maintained after the introduction of macropores, the SSAs were similar for all the prepared samples. Macroporous TWC particles with similar SSAs can therefore be successfully prepared with additions of PMMA as a template and by using a spray method and subsequently additional heating process.

The CO_2 adsorption performances of the as-prepared samples at 298.15 K in the pressure range of 0–110 kPa are shown in Fig. 7**(a)**. The results show that the adsorption capacities increased proportionally with increasing pressure. The Langmuir and Freundlich adsorption models were approached to investigate CO_2 adsorption properties on the porous TWC particles. The adsorption data of the prepared samples were fitted into Langmuir and Freundlich equations to determine which model give the best correlation to experimental data. The fitting and calculation data in **Figure S4** and **Table S1** (Supplementary material) show that the CO_2 adsorptions

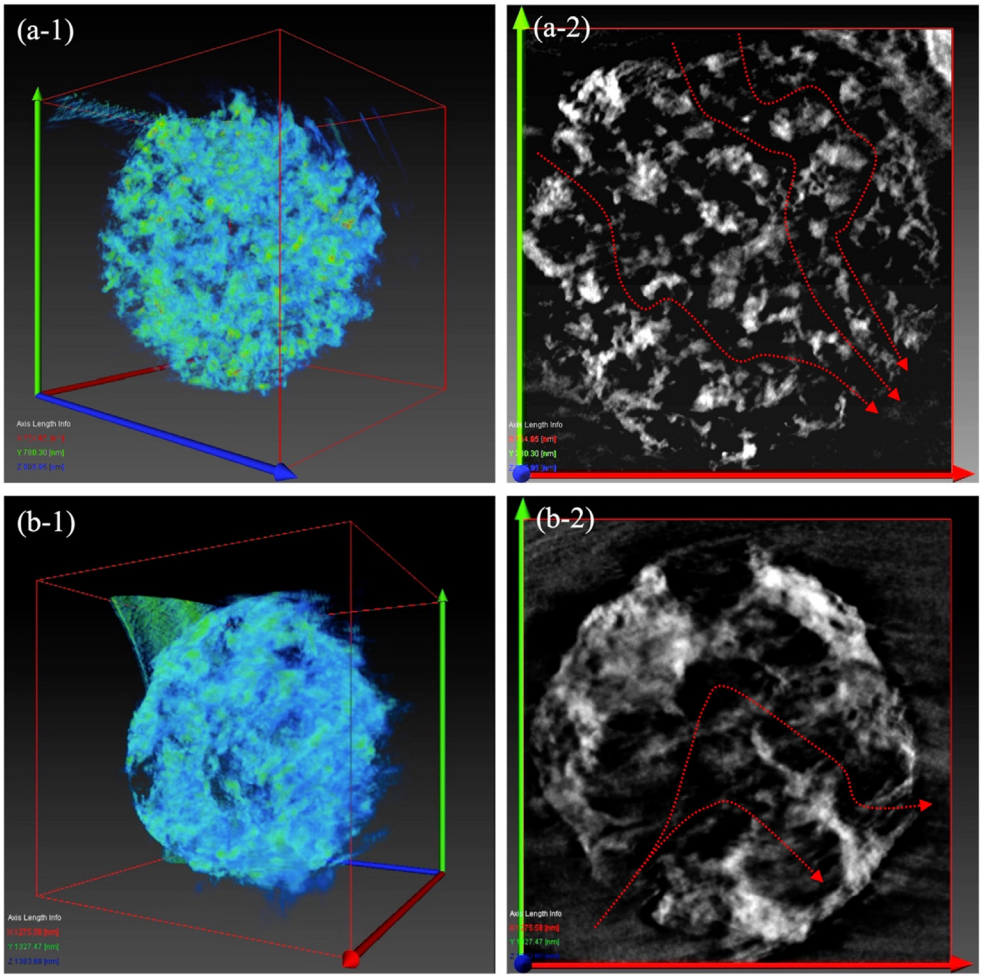

Fig. 5. TEM Tomography volume rendering images (left) and slice images (right) of **P1-TWC-H** (a) and **P2-TWC-H** (b). Red dotted arrows illustrate the gas transportations through the macroporous structures.

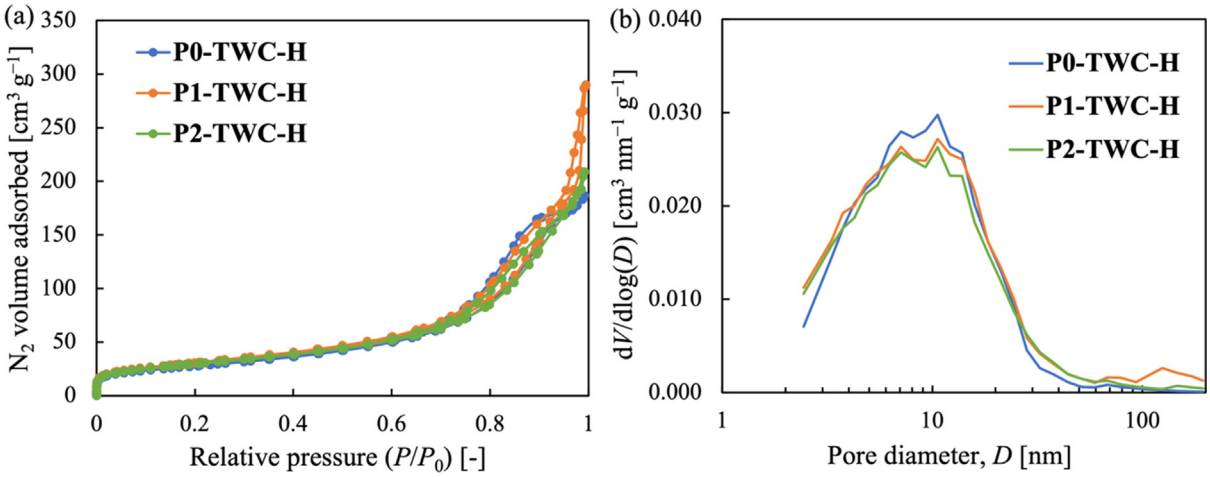

Fig. 6. N_2 adsorption–desorption isotherms (a) and pore size distributions (b) of **P0-TWC-H**, **P1-TWC-H**, and **P2-TWC-H**.

of as-prepared porous TWC particles follow the Freundlich model. As discussed in Supplementary material, the Freundlich adsorption model describes the heterogeneous adsorption of molecules on the adsorbent's surface without the limitation of an adsorption layer. The adsorption of CO_2 on the porous TWC materials can therefore be assumed to be the physisorption [44]. In physisorption, the adsorption capacity varies proportionally with the SSA of the adsorbent. Generally, an adsorbent with higher SSA possesses a higher adsorption capacity [45,46]. As previously discussed, the prepared porous TWC particles have similar SSA, which indicates that they possess similar CO_2 adsorption capacities (Fig. 7**(a)**). Although they have similar adsorption capacities, the adsorption

Table 2
Specific surface areas (SSAs), and micropore, mesopore, macropore, and total pore volumes of all prepared samples after additional heating process.

Sample	SSA [$m^2\ g^{-1}$]	V_{micro} [$cm^3\ g^{-1}$]	V_{meso} [$cm^3\ g^{-1}$]	V_{macro} [$cm^3\ g^{-1}$]	Total pore volume [$cm^3\ g^{-1}$]
P0-TWC-H	100	0.037	0.259	0.025	0.321
P1-TWC-H	112	0.041	0.271	0.136	0.448
P2-TWC-H	107	0.039	0.256	0.054	0.349

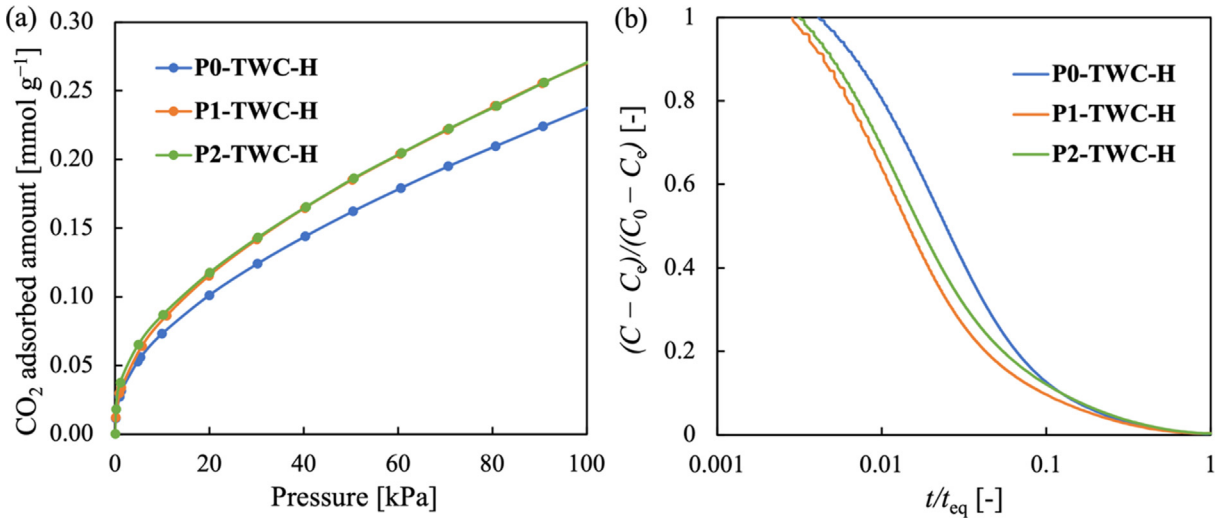

Fig. 7. CO_2 adsorption capacities (a) and CO_2 adsorption rates (b) of prepared porous TWC particles.

rates of the prepared samples differ because of structural differences among the particles. Fig. 7**(b)** shows the plots of $(C - C_e)/(C_0 - C_e)$ versus dimensionless time (t/t_{eq}; t is the adsorption time [s] and t_{eq} is the adsorption equilibrium time [s]) for the as-prepared samples. The results show that **P1-TWC-H** possesses the highest adsorption rate, **P0-TWC-H** has the lowest adsorption rate, and a moderate adsorption rate was **P2-TWC-H**. The LDF approximation was utilized to calculate the mass transfer coefficient (k_{LDF}) from the CO_2 adsorption rate; k_{LDF} determines the efficiency of CO_2 molecule transportation in the porous TWC particles.

Determination of the CO_2 adsorbed amount is an easy task. However, the mass transfer coefficient for the kinetic of adsorption rate was not easy to be calculated at constant volume and variable pressure. Many factors that can adversely affect the mass transfer coefficient calculation have been reported, e.g., the effect of adsorption heat, heat transfer to the surrounding environment, late time responses, and the pressure step size [47]. Taking into account all the previously described limitations, the mass transfer coefficient was calculated from selected CO_2 uptake rates by using a simple LDF approximation. For this purpose, only some experimental uptake rates at specific partial pressures were used to calculate the k_{LDF}, especially at the low pressure.

The adsorption rates and mass transfer coefficients were obtained at similar equilibrium pressures, and the results are shown in Table 3. The mass transfer coefficient of the macroporous sample (**P1-TWC-H**, $k_{LDF} = 1.04 \times 10^{-2}\ s^{-1}$) is higher than that of aggregate sample (**P0-TWC-H**, $k_{LDF} = 5.52 \times 10^{-3}\ s^{-1}$). This is because macropores promote gas transfer from the surface to the inner structure, which results in a faster adsorption rate and higher mass transfer coefficient. Whereas the mesopores, which are smaller sizes, limit gas transportation. These results indicate that the introduction of macropores enhances the mass transfer coefficient. However, the results in Table 3 show that further increases in the macropore size would decrease the mass transfer coefficient. The mass transfer coefficient ($k_{LDF} = 6.49 \times 10^{-3}\ s^{-1}$) of the macroporous sample (**P2-TWC-H**) prepared with PMMA 242 nm is lower than that of **P1-TWC-H** sample, which was prepared with PMMA 67 nm. The limitations of larger macropore size on gas transportation are shown in **Figure S5** (Supplementary material). A larger template provides larger macropores, and this results in a thicker wall between macropores. Because this thicker wall contains more mesopores, it limits the transportation of gas molecules to the adsorption sites, and decreases the adsorption rate and mass transfer coefficient. These results are consistent with those of the previous studies [23,48], in which molecules transportations in macropores of various sizes were simulated. Although macropores enhance mass transfer inside the porous structure, further increasing the macropore size limits gas transportation and decreases the mass transfer coefficient. Determination of the optimal macropores size for achieving the maximum mass transfer coefficient is therefore important. More experiments need to be performed to investigate the effects of different template sizes and others experimental parameters on the mass transfer efficiency.

Table 3
Mass transfer coefficients (k_{LDF}) of prepared TWC particles.

Sample	Equilibrium pressure [Pa]	Mass transfer coefficient [s^{-1}]
P0-TWC-H	158.8	5.52×10^{-3}
P1-TWC-H	139.7	1.04×10^{-2}
P2-TWC-H	185.3	6.49×10^{-3}

4. Conclusions

This report describes the synthesis of macroporous TWC particles via a template-assisted spray process followed by the additional heating process with the association of two templates, i.e., PMMA 67 and 242 nm. Spherical macroporous TWC particles were obtained when N_2 was used as the carrier gas. When air was used

instead of N_2, the PGM components in the TWC promoted PMMA decomposition in the presence of oxygen, which resulted in the broken porous TWC particles. The morphologies of the macroporous TWC particles were retained during the additional heating process. However, slight reductions in the particle size were observed because of particle shrinkage at high temperatures during the additional heating step. TEM Tomography 3D structures showed interconnected macroporous structures in the TWC particles prepared at a PMMA/TWC mass ratio of 1.0. The mass transfer coefficients were enhanced by introducing interconnected macropores into the TWC particles. Therefore, the mass transfer coefficient of the macroporous sample derived from PMMA 67 nm was higher than that of the aggregate sample. However, larger macropores decreased the mass transfer coefficient because of limitation of gas transfer to the adsorption sites. Overall, this study shows the benefits of using a PMMA template to control and design macroporous TWC particles to improve gas transportation inside the particles. These results suggest that macroporous TWC particles could be used in the commercial products for achieving lower exhaust emission levels. In future work, the macropores size will be further investigated to achieve the maximum mass transfer coefficient. Macroporous TWC particles could then be used to investigate removal of three main exhaust components to achieve a green environment.

Declaration of Competing Interest

The authors declare that they have no known competing financial interests or personal relationships that could have appeared to influence the work reported in this paper.

Acknowledgements

This research was supported by JSPS KAKENHI Grant Number 19H02500. This work is partly supported by the Center for Functional Nano Oxide at Hiroshima University, International Network on Polyoxometalate Science, JSPS Core-to-Core Program, the Information Center of Particle Technology, Japan, and the Hosokawa Powder Technology Foundation. We thank Dr. Makoto Maeda of the Natural Science Center for Basic Research and Development (N-BARD) at Hiroshima University for TEM observations and discussion. We also thank Helen McPherson, PhD, from Edanz (https://jp.edanz.com/ac) for editing a draft of this manuscript.

Appendix A. Supplementary material

Supplementary data to this article can be found online at https://doi.org/10.1016/j.apt.2022.103581.

References

[1] Y. Wang, H. Arandiyan, J. Scott, A. Bagheri, H. Dai, R. Amal, Recent advances in ordered meso/macroporous metal oxides for heterogeneous catalysis: A review, J. Mater. Chem. A 5 (2017) 8825–8846.
[2] L. Gradon, R. Balgis, T. Hirano, A.M. Rahmatika, T. Ogi, K. Okuyama, Advanced aerosol technologies towards structure and morphologically controlled next-generation catalytic materials, J. Aerosol Sci. 149 (2020) 105608.
[3] L.J. Broadbelt, R.Q. Snurr, Applications of molecular modeling in heterogeneous catalysis research, Appl. Catal. A 200 (2000) 23–46.
[4] D.P. Debecker, S. le Bras, C. Boissière, A. Chaumonnot, C. Sanchez, Aerosol processing: a wind of innovation in the field of advanced heterogeneous catalysts, Chem. Soc. Rev. 47 (2018) 4112–4155.
[5] C.M. Friend, B. Xu, Heterogeneous catalysis: A central science for a sustainable future, Acc. Chem. Res. 50 (2017) 517–521.
[6] M.E. Davis, Ordered porous materials for emerging applications, Nature 417 (2002) 813–821.
[7] A. Wittstock, V. Zielasek, J. Biener, C.M. Friend, M. Bäumer, Nanoporous gold catalysts for selective gas-phase oxidative coupling of methanol at low temperature, Science 327 (2010) 319–322.
[8] Q. Yang, Q. Xu, H.-L. Jiang, Metal–organic frameworks meet metal nanoparticles: synergistic effect for enhanced catalysis, Chem. Soc. Rev. 46 (2017) 4774–4808.
[9] C. Zhu, D. Du, A. Eychmüller, Y. Lin, Engineering ordered and nonordered porous noble metal nanostructures: Synthesis, assembly, and their applications in electrochemistry, Chem. Rev. 115 (2015) 8896–8943.
[10] Z. Dai, T. Liang, J.H. Lee, Gas sensors using ordered macroporous oxide nanostructures, Nanoscale Adv. 1 (2019) 1626–1639.
[11] Y. Wu, F. Li, W. Zhu, J. Cui, C. Tao, C. Lin, P.M. Hannam, G. Li, Metal-organic frameworks with a three-dimensional ordered macroporous structure: dynamic photonic materials, Angew. Chem. 123 (2011) 12726–12730.
[12] O.H. Kim, Y.H. Cho, S.H. Kang, H.Y. Park, M. Kim, J.W. Lim, D.Y. Chung, M.J. Lee, H. Choe, Y.E. Sung, Ordered macroporous platinum electrode and enhanced mass transfer in fuel cells using inverse opal structure, Nat. Commun. 4 (2013) 1–9.
[13] O. Arutanti, A.F. Arif, R. Balgis, T. Ogi, K. Okuyama, F. Iskandar, Tailored synthesis of macroporous Pt/WO_3 photocatalyst with nanoaggregates via flame assisted spray pyrolysis, AIChE J. 62 (2016) 3864–3873.
[14] O. Arutanti, A.B.D. Nandiyanto, T. Ogi, T.O. Kim, K. Okuyama, Influences of porous structurization and Pt addition on the improvement of photocatalytic performance of WO_3 particles, ACS Appl. Mater. Interfaces 7 (2015) 3009–3017.
[15] F. Iskandar, A.B.D. Nandiyanto, K.M. Yun, C.J. Hogan, K. Okuyama, P. Biswas, Enhanced photocatalytic performance of Brookite TiO_2 macroporous particles prepared by spray drying with colloidal templating, Adv. Mater. 19 (2007) 1408–1412.
[16] R. Balgis, W. Widiyastuti, T. Ogi, K. Okuyama, Enhanced electrocatalytic activity of Pt/3D hierarchical bimodal macroporous carbon nanospheres, ACS Appl. Mater. Interfaces 9 (2017) 23792–23799.
[17] R. Balgis, A.F. Arif, T. Mori, T. Ogi, K. Okuyama, G.M. Anilkumar, Morphology-dependent electrocatalytic activity of nanostructured Pt/C particles from hybrid aerosol-colloid process, AIChE J. 62 (2016) 440–450.
[18] R. Balgis, T. Ogi, A.F. Arif, G.M. Anilkumar, T. Mori, K. Okuyama, Morphology control of hierarchical porous carbon particles from phenolic resin and polystyrene latex template via aerosol process, Carbon 84 (2015) 281–289.
[19] A.M. Rahmatika, Y. Goi, T. Kitamura, W. Widiyastuti, T. Ogi, TEMPO-oxidized cellulose nanofiber (TOCN) decorated macroporous silica particles: Synthesis, characterization, and their application in protein adsorption, Mater. Sci. Eng., C 105 (2019) 110033.
[20] A.M. Rahmatika, Y. Goi, T. Kitamura, Y. Morita, F. Iskandar, T. Ogi, Silica-supported carboxylated cellulose nanofibers for effective lysozyme adsorption: Effect of macropore size, Adv. Powder Technol. 31 (2020) 2932–2941.
[21] A.M. Rahmatika, Y. Toyoda, T.T. Nguyen, Y. Goi, T. Kitamura, Y. Morita, K. Kume, T. Ogi, Cellulose nanofiber and magnetic nanoparticles as building blocks constructing biomass-based porous structured particles and their protein adsorption performance, ACS Sustainable Chem. Eng. 8 (2020) 18686–18695.
[22] X. Zheng, G. Shen, C. Wang, Y. Li, D. Dunphy, T. Hasan, C.J. Brinker, B.L. Su, Bio-inspired Murray materials for mass transfer and activity, Nat. Commun. 8 (2017) 1–9.
[23] L. Yang, H. Cao, Y. Yue, C. Yang, H. Liu, T. Wang, X. Bao, Diffusion simulation based design and macroporous structure tailored preparation of FCC naphtha selective hydrodesulfurization catalyst, Fuel Process. Technol. 208 (2020) 106498.
[24] S. Rood, S. Eslava, A. Manigrasso, C. Bannister, Recent advances in gasoline three-way catalyst formulation: a review, Proc. Instit. Mech. Eng. Part D: J. Automobile Eng. 234 (2020) 936–949.
[25] C. Huang, W. Shan, Z. Lian, Y. Zhang, H. He, Recent advances in three-way catalysts of natural gas vehicles, Catal. Sci. Technol. 10 (2020) 6407–6419.
[26] A.M. Beale, F. Gao, I. Lezcano-Gonzalez, C.H.F. Peden, J. Szanyi, Recent advances in automotive catalysis for NO_x emission control by small-pore microporous materials, Chem. Soc. Rev. 44 (2015) 7371–7405.
[27] A.A. Vedyagin, M.S. Gavrilov, A.M. Volodin, V.O. Stoyanovskii, E.M. Slavinskaya, I.V. Mishakov, Y.V. Shubin, Catalytic purification of exhaust gases over Pd–Rh alloy catalysts, Top. Catal. 56 (2013) 1008–1014.
[28] J. Wang, J. Wen, M. Shen, Effect of interaction between $Ce_{0.7}Zr_{0.3}O_2$ and Al_2O_3 on structural characteristics, thermal stability, and oxygen storage capacity, J. Phys. Chem. C 112 (2008) 5113–5122.
[29] S. Li, X. Li, Y. Dan, Y. Jiao, J. Deng, L. Xiong, J. Wang, Y. Chen, Designed synthesis of nanostructured Al_2O_3 stabilized homogeneous CeO_2-ZrO_2 solid solution as highly active support for Pd-only three-way catalyst, Mol. Catal. 477 (2019) 110513.
[30] S.L. Winkler, J.E. Anderson, L. Garza, W.C. Ruona, R. Vogt, T.J. Wallington, Vehicle criteria pollutant (PM, NO_x, CO, HCs) emissions: how low should we go?, NPJ Clim Atmos. Sci. 1 (2018) 26.
[31] A.B.D. Nandiyanto, T. Ogi, W.N. Wang, L. Gradon, K. Okuyama, Template-assisted spray-drying method for the fabrication of porous particles with tunable structures, Adv. Powder Technol. 30 (2019) 2908–2924.
[32] T. Ogi, A.B.D. Nandiyanto, K. Okuyama, Nanostructuring strategies in functional fine-particle synthesis towards resource and energy saving applications, Adv. Powder Technol. 25 (2014) 3–17.
[33] A.F. Arif, R. Balgis, T. Ogi, T. Mori, K. Okuyama, Experimental and theoretical approach to evaluation of nanostructured carbon particles derived from phenolic resin via spray pyrolysis, Chem. Eng. J. 271 (2015) 79–86.

[34] S.I. Nakao, M. Suzuki, Mass transfer coefficient in cyclic adsorption and desorption, J. Chem. Eng. Jpn. 16 (1983) 114–119.
[35] S.B. Kang, S.J. Han, I.S. Nam, B.K. Cho, C.H. Kim, S.H. Oh, Detailed reaction kinetics for double-layered Pd/Rh bimetallic TWC monolith catalyst, Chem. Eng. J. 241 (2014) 273–287.
[36] H. Nakayama, M. Nagata, H. Abe, Y. Shimizu, In Situ TEM study of Rh particle sintering for three-way catalysts in high temperatures, Catalysts 11 (2021) 1–16.
[37] Q. Xu, K.C. Kharas, B.J. Croley, A.K. Datye, The sintering of supported Pd automotive catalysts, ChemCatChem 3 (2011) 1004–1014.
[38] A.B. Dani Nandiyanto, Y. Kito, T. Hirano, R. Ragadhita, P.H. Le, T. Ogi, Spherical submicron YAG: Ce particles with controllable particle outer diameters and crystallite sizes and their photoluminescence properties, RSC Adv. 11 (2021) 30305–30314.
[39] Z.Y. Yuan, B.L. Su, Insights into hierarchically meso-macroporous structured materials, J. Mater. Chem. 16 (2006) 663–677.
[40] K.L.A. Cao, Y. Kitamoto, F. Iskandar, T. Ogi, Sustainable porous hollow carbon spheres with high specific surface area derived from Kraft lignin, Adv. Powder Technol. 32 (2021) 2064–2073.
[41] T.T. Nguyen, A.M. Rahmatika, M. Miyauchi, K.L.A. Cao, T. Ogi, Synthesis of high specific surface area macroporous pectin particles by template-assisted spray drying, Langmuir 37 (2021) 4256–4266.
[42] K.L.A. Cao, A.M. Rahmatika, Y. Kitamoto, M.T.T. Nguyen, T. Ogi, Controllable synthesis of spherical carbon particles transition from dense to hollow structure derived from Kraft lignin, J. Colloid Interface Sci. 589 (2021) 252–263.
[43] Y. Kitamoto, K.L.A. Cao, P.H. Le, O.B. Abdillah, F. Iskandar, T. Ogi, A Sustainable approach for preparing porous carbon spheres derived from Kraft lignin and sodium hydroxide as highly packed thin film electrode materials, Langmuir 38 (2022) 3540–3552.
[44] N.A. Rashidi, S. Yusup, A. Borhan, Isotherm and thermodynamic analysis of carbon dioxide on activated carbon, Procedia Eng. 148 (2016) 630–637.
[45] M. Pardakhti, T. Jafari, Z. Tobin, B. Dutta, E. Moharreri, N.S. Shemshaki, S. Suib, R. Srivastava, Trends in solid adsorbent materials development for CO_2 capture, ACS Appl. Mater. Interfaces 11 (2019) 34533–34559.
[46] F. Hussin, M.K. Aroua, Recent trends in the development of adsorption technologies for carbon dioxide capture: A brief literature and patent reviews (2014–2018), J. Cleaner Prod. 253 (2020) 119707.
[47] M. Karimi, A.E. Rodrigues, J.A.C. Silva, Designing a simple volumetric apparatus for measuring gas adsorption equilibria and kinetics of sorption. Application and validation for CO_2, CH_4 and N_2 adsorption in binder-free beads of 4A zeolite, Chem. Eng. J. 425 (2021) 130538.
[48] Y. Lin, C. Yang, Z. Wan, T. Qiu, Lattice Boltzmann simulation of intraparticle diffusivity in porous pellets with macro-mesopore structure, Int. J. Heat Mass Transf. 138 (2019) 1014–1028.